

# Formation of carbonyl sulfide (OCS) via SH radicals in interstellar CO-rich ice under dense cloud conditions

J. C. Santos<sup>1</sup>, H. Linnartz<sup>1,2</sup>, and K.-J. Chuang<sup>1</sup>

<sup>1</sup> Laboratory for Astrophysics, Leiden Observatory, Leiden University, PO Box 9513, 2300 RA Leiden, The Netherlands  
e-mail: santos@strw.leidenuniv.nl

<sup>2</sup> Deceased, 31/12/2023

August 9, 2024

## ABSTRACT

**Context.** Carbonyl sulfide (OCS) is widely observed in the gas phase towards star-forming regions and was the first of the only two sulfur-bearing species detected in interstellar ices so far. However, the chemical network governing its formation is still not fully understood. While the sulfurization of CO and the oxidation of CS are often invoked to form OCS, other mechanisms could have a significant contribution. In particular, the multistep reaction involving CO and SH is a good candidate to forming OCS in dense cloud environments.

**Aims.** We aim to constrain the viability of the CO + SH route to forming solid OCS in the interstellar medium, in a similar manner as CO + OH is known to produce CO<sub>2</sub> ice. This is achieved by conducting a systematic laboratory investigation of the targeted reactions on interstellar ice analogues under dense cloud conditions.

**Methods.** An ultrahigh vacuum chamber is utilized to simultaneously deposit CO, H<sub>2</sub>S, and atomic H at 10 K. SH radicals produced in situ via hydrogen abstraction from H<sub>2</sub>S react with CO to form OCS. The ice composition during deposition and subsequent warm-up is monitored by means of Fourier-transform reflection absorption infrared spectroscopy (RAIRS). Complementarily, desorbed species are recorded with a quadrupole mass spectrometer (QMS) during temperature-programmed desorption (TPD) experiments. Control experiments are performed to secure the product identification. The effect of different H<sub>2</sub>S:CO mixing ratios, with decreasing H<sub>2</sub>S concentrations, on the OCS formation yield is also explored.

**Results.** OCS is efficiently formed through surface reactions involving CO, H<sub>2</sub>S, and H atoms. The suggested underlying mechanism behind OCS formation is CO + SH → HSCO followed by HSCO + H → OCS + H<sub>2</sub>. The OCS yield reduces slowly, but remains significant with increasing CO:H<sub>2</sub>S mixing ratios (CO:H<sub>2</sub>S = 1:1, 5:1, 10:1, and 20:1).

**Conclusions.** Our experiments provide unambiguous evidence that OCS can be formed from CO + SH in the presence of H atoms. This route remains efficient for large H<sub>2</sub>S dilutions (5% w.r.t CO), suggesting that it is a viable mechanism in interstellar ices. Given that SH radicals can be created in clouds throughout a wide evolutionary timescale, this mechanism could have a non-negligible contribution to forming interstellar OCS ice.

**Key words.** Astrochemistry, Methods: laboratory: solid state, Infrared: ISM, ISM: molecules

## 1. Introduction

Among the over 300 molecules detected in the interstellar medium to date<sup>1</sup>, those that contain sulfur constitute one of the most conspicuous chemical families. They are observed in the gas phase throughout a wide evolutionary time span, from clouds (e.g., Drdla et al. 1989; Navarro-Almida et al. 2020; Spezzano et al. 2022; Esplugues et al. 2022) to protostars (e.g., Blake et al. 1987, 1994; van der Tak et al. 2003; Li et al. 2015; Drozdovskaya et al. 2018; Codella et al. 2021; Artur de la Villarmois et al. 2023; Fontani et al. 2023; Kushwahaa et al. 2023), protoplanetary disks (Fuente et al. 2010; Phuong et al. 2018; Semenov et al. 2018; Le Gal et al. 2019; Rivière-Marichalar et al. 2021; Le Gal et al. 2021; Booth et al. 2024), and solar-system bodies (Smith et al. 1980; Bockelée-Morvan et al. 2000; Hibbitts et al. 2000; Jessup et al. 2007; Moullet et al. 2008, 2013; Cartwright et al. 2020; Biver et al. 2021a,b; Calmonte et al. 2016; Altwegg et al. 2022). The hitherto detected species range in size, from simple diatomic molecules such as CS and SO to the thiols CH<sub>3</sub>SH and CH<sub>3</sub>CH<sub>2</sub>SH (Linke et al. 1979; Gibb et al. 2000; Cernicharo

et al. 2012; Kolesníková et al. 2014; Zapata et al. 2015; Müller et al. 2016; Majumdar et al. 2016; Rodríguez-Almeida et al. 2021).

As opposed to gas-phase observations, however, only two sulfurated molecules have been detected in interstellar ices to date: OCS and SO<sub>2</sub> (Palumbo et al. 1995; Boogert et al. 1997; Palumbo et al. 1997; Öberg et al. 2008; Boogert et al. 2022; McClure et al. 2023; Rocha et al. 2024). This is probably in large part due to their low abundances combined with the intrinsic limitations of solid-state observations, such as the broadness of the features and their high degeneracy. Nonetheless, these confirmed ice species already bring vast chemical ramifications since they can act as reactants to form more complex organosulfur compounds, some of which with key biochemical roles (see, e.g., McAnally et al. 2024). Yet, despite their astrochemical significance, many open questions still remain regarding the formation pathways for these small sulfur-bearing molecules in the solid-state.

One particularly important case is that of carbonyl sulfide (OCS). It is a major gaseous sulfur carrier, commonly detected towards young stellar objects (e.g., van der Tak et al. 2003; Herpin et al. 2009; Oya et al. 2016; Drozdovskaya et al. 2018; Kush-

<sup>1</sup> <https://cdms.astro.uni-koeln.de/>

wahaa et al. 2023; López-Gallifa et al. 2024; Santos et al. submitted). It is also frequently detected in interstellar ices (see, e.g., Palumbo et al. 1997; Boogert et al. 2022), in part facilitated by the characteristically large absorption band strength of its  $4.9\ \mu\text{m}$  feature in comparison to other ice species (e.g.,  $\sim 1.2 \times 10^{-16}\ \text{cm molecule}^{-1}$  as measured by Yarnall & Hudson 2022 for pure OCS ice at 10 K; See also Hudgins et al. 1993). Observed OCS abundances in both protostellar ices and hot-core gas point to a solid-state formation mechanism occurring predominately during the high-density pre-stellar core stage ( $A_V > 9$ ,  $n_H \gtrsim 10^5\ \text{cm}^{-3}$ ), after the onset of the CO catastrophic freeze-out (Palumbo et al. 1997; Boogert et al. 2022; Santos et al. submitted). This proposed icy origin of OCS is corroborated by gas-phase astrochemical models, which fail to reproduce observed OCS abundances (Loison et al. 2012). In the inner regions of the protostellar envelope, thermal heating by the protostar causes the volatile ice content to fully sublimate, enabling the bulk of the gaseous OCS observations.

So far, the two most commonly proposed routes to OCS involve either the oxidation of CS or the sulfurization of CO in the solid state (Palumbo et al. 1997; Ferrante et al. 2008; Adriaens et al. 2010; Chen et al. 2015; Laas & Caselli 2019; Shingledecker et al. 2020; Boogert et al. 2022):



However, CS abundances are considerably smaller ( $\lesssim 2.5\%$ ) than those of OCS, casting doubts on the extent of the contribution from Reaction 1 to the interstellar OCS content (Boogert et al. 2022). Reaction 2 is more often invoked as the dominant route to OCS, especially due to the large availability of solid-state CO as a reactant in the post freeze-out stage.

Hydrogen in its atomic form is also abundant in pre-stellar cores ( $\text{H}/\text{CO} \sim 1\text{--}10$ , Lacy et al. 1994; Goldsmith & Li 2005) and can trigger solid-state reactions of relevance to the sulfur network. Following adsorption onto dust grains, sulfur atoms are subject to successive hydrogenation reactions to form SH and  $\text{H}_2\text{S}$  via the steps:

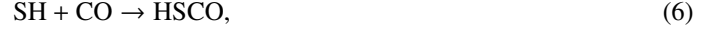


both of which are predicted by astrochemical models to proceed very efficiently (see, e.g., Garrod et al. 2007; Druard & Wakelam 2012; Esplugues et al. 2014; Vidal et al. 2017). Once  $\text{H}_2\text{S}$  ice is formed, it can further react with another hydrogen atom via an abstraction route (Lamberts & Kästner 2017; Oba et al. 2018, 2019; Santos et al. 2023), or be dissociated through energetic processing (e.g., Jiménez-Escobar et al. 2014; Chen et al. 2015; Cazaux et al. 2022):



thus partially replenishing the SH ice content. As a result, SH radicals will likely be present in the ice throughout a wide evolutionary time span, and could potentially serve as an alternative source of sulfur to forming OCS.

A particularly promising pathway is the reaction between SH and CO followed by a hydrogen abstraction step (Adriaens et al. 2010; Chen et al. 2015):



which involves the formation of the intermediate complex HSCO. This pathway is analogous to the case of  $\text{CO}_2$  ice formation from CO and OH through the HOCO complex (e.g., Oba et al. 2010; Ioppolo et al. 2011; Noble et al. 2011; Qasim et al. 2019; Molpeceres et al. 2023). In the case of  $\text{CO}_2$ , Molpeceres et al. (2023) find that the spontaneous dissociation of HOCO into H and  $\text{CO}_2$  is not energetically viable, and thus the formation of the latter is only possible through the interaction of the HOCO intermediate with a hydrogen atom. Similarly, HSCO is also prevented from spontaneously dissociating into OCS and H (Adriaens et al. 2010). In the laboratory, OCS is readily formed in energetically-processed  $\text{CO}:\text{H}_2\text{S}$  ice mixtures (Ferrante et al. 2008; Garozzo et al. 2010; Jiménez-Escobar et al. 2014; Chen et al. 2015), for which both reactions involving  $\text{CO} + \text{S}$  and  $\text{CO} + \text{SH}$  have been suggested as possible formation routes. Moreover, Nguyen et al. (2021) allude to the possibility of forming OCS through reactions 6 and 7 in a  $\text{CO}:\text{H}_2\text{S}$  ice mixture exposed to hydrogen atoms, albeit without exploring it further. Dedicated laboratory studies focused on assessing this particular reaction pathway to OCS formation are therefore still highly warranted.

In this experimental work, we investigate the viability of OCS formation via Reactions 6 and 7 under dark cloud conditions by depositing simultaneously  $\text{H}_2\text{S}$ , CO, and H atoms at 10 K. The SH radicals are produced via Reaction 5a, and are subsequently subject to reacting with neighboring species. The experimental methods utilized in this work are described in Section 2. In Section 3, we present and discuss our main results. Their astrophysical implications are elaborated in Section 4, followed by a summary of our main findings in Section 5.

## 2. Experimental methods

This work utilizes the ultrahigh vacuum (UHV) setup SURFRESIDE<sup>3</sup>, for which detailed descriptions are provided elsewhere (Ioppolo et al. 2013; Qasim et al. 2020). In a nutshell, this setup contains a main chamber that operates at base pressures of  $\sim 5 \times 10^{-10}$  mbar, and at the center of which a gold-plated copper substrate is mounted on the tip of a closed-cycle helium cryostat. Resistive heaters are used to vary the substrate temperature between 8 and 450 K, as monitored by two silicon diode sensors with a relative accuracy of 0.5 K. A hydrogen atom beam source (HABS Tschersich 2000) generates H atoms that are subsequently cooled down by colliding with a nose-shaped quartz pipe before reaching the substrate. Simultaneously to in-letting H atoms into the chamber, gases of  $\text{H}_2\text{S}$  (Linde, 99.5% purity) and CO (Linde, 99.997% purity) are concomitantly admitted through two separate all-metal leak valves. The heavier isotopologue  $^{13}\text{C}^{18}\text{O}$  (Sigma-Aldrich, 95% purity

**Table 1.** Experiments performed in this work.

Experiment	Label	CO flux ( $\text{cm}^{-2} \text{ s}^{-1}$ )	H <sub>2</sub> S flux ( $\text{cm}^{-2} \text{ s}^{-1}$ )	H flux ( $\text{cm}^{-2} \text{ s}^{-1}$ )	CO:H <sub>2</sub> S:H
CO + H <sub>2</sub> S + H	1	$1.8 \times 10^{11}$	$1.8 \times 10^{11}$	$5.5 \times 10^{12}$	1:1:30
CO + H <sub>2</sub> S	2	$1.8 \times 10^{11}$	$1.8 \times 10^{11}$	–	1:1:0
<sup>13</sup> C <sup>18</sup> O + H <sub>2</sub> S + H	3	$1.8 \times 10^{11}$	$1.8 \times 10^{11}$	$5.5 \times 10^{12}$	1:1:30
CO + H <sub>2</sub> S + H	4	$9.3 \times 10^{11}$	$1.8 \times 10^{11}$	$5.5 \times 10^{12}$	5:1:30
CO + H <sub>2</sub> S + H	5	$1.8 \times 10^{12}$	$1.8 \times 10^{11}$	$5.5 \times 10^{12}$	10:1:30
CO + H <sub>2</sub> S + H	6	$3.7 \times 10^{12}$	$1.8 \times 10^{11}$	$5.5 \times 10^{12}$	20:1:30

<sup>18</sup>O, 99% purity <sup>13</sup>C) is also utilized to assist in the product identification. Fourier-transform reflection-absorption infrared spectroscopy (FT-RAIRS) is used to monitor ice growth in the range of 700 to 4000  $\text{cm}^{-1}$  with 1  $\text{cm}^{-1}$  spectral resolution. When the deposition is complete, temperature-programmed desorption experiments (TPD) are performed by heating the sample at a constant rate of 5 K  $\text{min}^{-1}$ . During TPD, the solid phase is monitored by RAIRS, while the sublimated species are immediately ionized by 70 eV electron impact and are recorded by a quadrupole mass spectrometer (QMS). The variation of the substrate temperature during the collection of each IR TPD spectrum is of  $\sim 10$  K.

The absolute abundance of the ice species can be derived from their integrated infrared absorbance ( $\int Abs(\nu) d\nu$ ) using a modified Beer-Lambert law:

$$N_X = \ln 10 \frac{\int Abs(\nu) d\nu}{A'(X)} \quad (8)$$

where  $N_X$  is the column density in molecules  $\text{cm}^{-2}$  and  $A'(X)$  is the apparent absorption band strength in  $\text{cm molecule}^{-1}$  of a given species. We utilize  $A'(\text{CO})_{\sim 2142 \text{ cm}^{-1}} \sim (4.2 \pm 0.3) \times 10^{-17}$   $\text{cm molecule}^{-1}$  and  $A'(\text{H}_2\text{S})_{\sim 2553 \text{ cm}^{-1}} \sim (4.7 \pm 0.1) \times 10^{-17}$   $\text{cm molecule}^{-1}$ , as measured for our reflection-mode IR settings using the laser-interference technique (see Santos et al. 2023 for the case of H<sub>2</sub>S). For the target product, OCS, we employ the band strength of  $A'(\text{OCS})_{\sim 2043 \text{ cm}^{-1}} \sim (1.2 \pm 0.1) \times 10^{-16}$   $\text{cm molecule}^{-1}$  measured in transmission mode by Yarnall & Hudson (2022), and correct it by an averaged transmission-to-reflection conversion factor of 3.2 derived with our experimental setup (see Santos et al. 2023 for the case of H<sub>2</sub>S, which was later combined with CO ice depositions to derive the averaged setup-specific conversion factor).

Table 1 summarizes the experiments performed in this work. All depositions are carried out for 180 minutes with a constant substrate temperature of 10 K. The relative errors of the H-atom flux, as well as both molecule fluxes, are estimated to be  $\lesssim 5\%$ . The latter are estimated from evaluating the ice growth rate in multiple pure ice deposition experiments. To estimate the former, multiple experiments to calibrate the relative H-atom flux are conducted. These consist of trapping H atoms inside O<sub>2</sub> ice matrices and monitoring the formation of HO<sub>2</sub>, which is proportional to the H-atom flux provided that O<sub>2</sub> is overabundant relative to H (Ioppolo et al. 2013; Fedoseev et al. 2015). The instrumental uncertainties in the integrated QMS and IR signals are derived from the corresponding integrated spectral noise for the same band width.

### 3. Results and discussion

#### 3.1. OCS formation

Panel a) of Figure 1 shows the infrared spectra obtained after codeposition of CO, H<sub>2</sub>S, and H atoms (1:1:30, experiment 1) at 10 K, as well as after a control experiment of only CO and H<sub>2</sub>S (1:1, experiment 2). When CO and H<sub>2</sub>S are exposed to hydrogen atoms, a new feature appears at  $\sim 2043 \text{ cm}^{-1}$  ( $\sim 4.89 \mu\text{m}$ ) with a full-width at half maximum (FWHM) of  $\sim 15 \text{ cm}^{-1}$  ( $\sim 0.03 \mu\text{m}$ ). Based on its peak position and the ice elemental composition (i.e., C, O, S, and H), this feature is assigned as the CO-stretching mode of OCS ( $\nu_1$ , Yarnall & Hudson 2022)<sup>2</sup>. The band's FWHM and peak position are also consistent with previously reported values for OCS in CO-rich ices measured in reflection mode (Ferrante et al. 2008). To confirm this assignment, an analogous experiment is performed with a heavier isotopologue of carbon monoxide, <sup>13</sup>C<sup>18</sup>O (experiment 3, blue spectrum in Figure 1). In this case, the <sup>18</sup>O<sup>13</sup>C  $\nu_1$  feature appears at  $\sim 1954 \text{ cm}^{-1}$  ( $\sim 5.12 \mu\text{m}$ ) in accordance with the expected redshift of the heavier isotopologue. During TPD, both features at  $\sim 2043 \text{ cm}^{-1}$  and  $\sim 1954 \text{ cm}^{-1}$  disappear from the ice in the same temperature interval of 70–100 K (Panels b) and c) in Figure 1), thus signaling that the two bands correspond to the same molecule.

Complementarily to the infrared spectra, data obtained by the QMS during TPD can also be used to strengthen the OCS identification. Panel a) of Figure 2 displays the signal for  $m/z = 60$  recorded during the warm-up of the ice sample in the CO + H<sub>2</sub>S + H experiment. This mass-to-charge ratio corresponds to the molecular ion of OCS, its strongest signal resulting from 70 eV electron impact as listed in NIST<sup>3</sup>. A desorption feature appears peaking at  $\sim 89$  K, in agreement with previously reported desorption temperatures of OCS (Ferrante et al. 2008; Nguyen et al. 2021). In the isotope-labeled experiment, a similar desorption peak is observed for  $m/z = 63$ , consistent with the mass shift corresponding to the molecular ion of <sup>18</sup>O<sup>13</sup>C<sup>18</sup>S. Moreover, no peak signal is detected for  $m/z = 60$ , indicating that this same feature appearing in experiment 1 corresponds uniquely to carbonyl sulfide. The desorption temperature of OCS as measured by the QMS correlates with the disappearance of the  $\sim 2043 \text{ cm}^{-1}$  feature in the infrared spectra taken during TPD, as evinced by the area of this infrared band as a function of substrate temperature (Figure 2 panel b). Both the infrared and QMS data therefore provide unequivocal evidence for the formation of OCS as a result of interactions between H<sub>2</sub>S, CO, and H atoms in the solid state.

<sup>2</sup> The numbers assigned to the CS and CO stretches of OCS are interchangeable. In this work, we adopt the notation from Yarnall & Hudson (2022).

<sup>3</sup> <https://webbook.nist.gov/chemistry/>

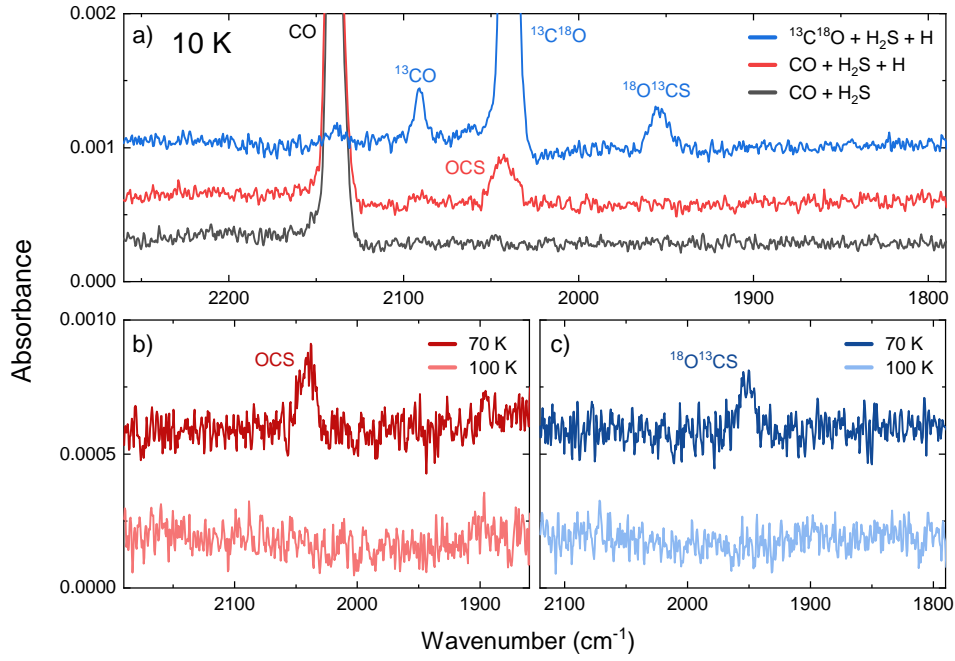


**Fig. 1.** Infrared data that confirms the formation of OCS from CO, H<sub>2</sub>S, and H atoms. Panel a): Spectrum collected after deposition of CO+H<sub>2</sub>S+H (experiment 1, red) together with the control experiment without H atoms (experiment 2, grey) and the isotope-labeled experiment with <sup>13</sup>C<sup>18</sup>O (experiment 3, blue). Small features assigned to <sup>13</sup>CO and <sup>12</sup>CO are due to minor contaminations from the gas bottle (respectively, ~ 4% and ~ 2% with respect to <sup>13</sup>C<sup>18</sup>O). Panel b): Infrared spectra acquired during TPD following the deposition of experiment 1. The spectrum in dark red (upper) is taken at ~70 K, and the one in light red (lower) is taken at ~100 K. Panel c): Same as panel b), but for the isotope-labeled experiment. In all panels only the relevant frequency range is shown and the spectra are offset for clarity.

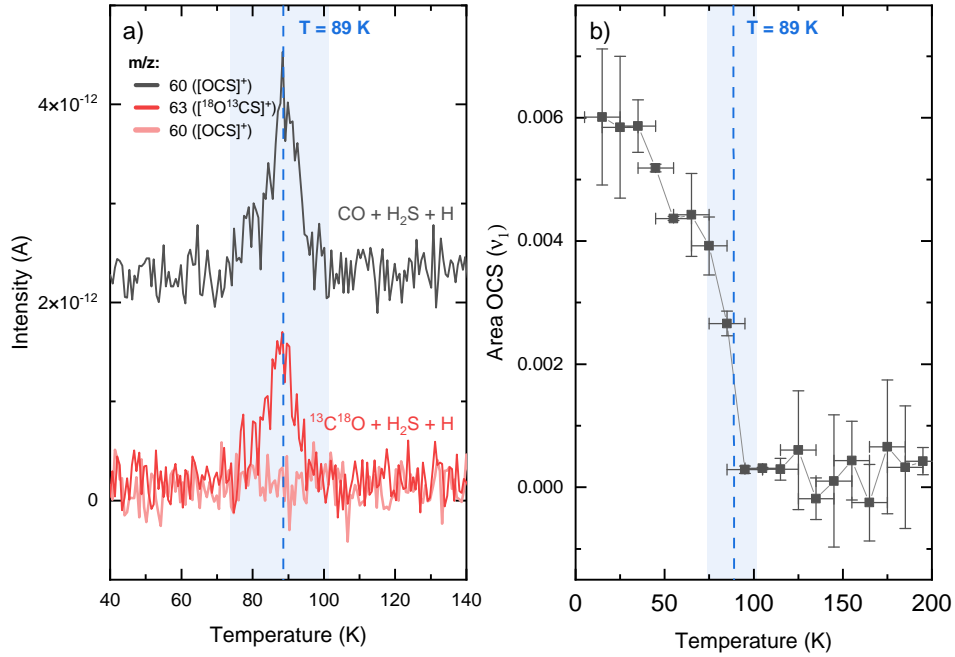


**Fig. 2.** Complementary QMS and infrared data acquired during TPD that confirms the OCS detection. Panel a): TPD-QMS signal recorded for  $m/z = 60$  after the deposition of CO + H<sub>2</sub>S + H (experiment 1, grey), as well as those for  $m/z = 63$  (dark red) and  $m/z = 60$  (light red) after the deposition of <sup>13</sup>C<sup>18</sup>O + H<sub>2</sub>S + H (experiment 3). The blue shadowed region denotes the range of desorption, and the dashed line highlights the peak desorption temperature. Signals from different experiments are offset for clarity. Panel b): Area of the OCS  $\nu_1$  band as a function of temperature during TPD following the deposition of experiment 1. The uncertainties in the horizontal axis are due to the substrate temperature variation of ~10 K during the collection of each IR TPD spectrum. The blue shadowed area and dashed line are reproductions of the range and peak position shown in Panel a).

Aside from OCS, another S-bearing species that could presumably be formed under our experimental conditions is thioformic acid, HCOSH. Indeed, formation routes via either the

hydrogenation of the HSCO intermediate or the interaction between HCO + SH have been proposed by Rodríguez-Almeida et al. (2021) to explain HCOSH observations towards the gi-

ant molecular cloud G+0.693–0.027, the former of which was later verified theoretically by Molpeceres et al. (2021). Although HCOSH has been shown to form upon keV electron irradiation of H<sub>2</sub>S:CO ices (Wang et al. 2022), Nguyen et al. (2021) only tentatively identify this product in similar hydrogenation experiments on H<sub>2</sub>S:CO ices. No evidence for this species is observed in our experiments above the instrumental detection limit. Likewise, we do not detect any signal of volatile sulfur allotropes such as S<sub>2</sub> or S<sub>3</sub>, nor of hydrogenated sulfur chains such as H<sub>2</sub>S<sub>2</sub> or H<sub>2</sub>S<sub>3</sub>—which could presumably be formed from the association of sulfur atoms produced via hydrogen abstraction reactions from SH radicals. This leads to the conclusion that the potential production of atomic S does not proceed efficiently under our experimental conditions. Moreover, since no H<sub>2</sub>S<sub>2</sub> is detected, the recombination of two SH radicals is also likely not efficient in the present experiments—signaling that HS radicals are efficiently consumed, both by reacting with CO leading to OCS and by reacting with H to reform H<sub>2</sub>S.

Reactions 6 and 7 are therefore the predominant contributors to forming OCS in our experiments. As shown by Nguyen et al. (2021), however, the backward reactions are also viable. Once formed, OCS can be hydrogenated into the complex intermediate HSCO, which in turn can further react with another H atom to yield CO and H<sub>2</sub>S, as well as dissociate back into the reactants SH and CO (Adriaens et al. 2010; Nguyen et al. 2021; Molpeceres et al. 2021). The effective amount of OCS detected will, therefore, be subject to these two competing directions.

### 3.2. Effects of larger CO fractions

Once the possibility of forming OCS from CO and SH is ascertained, the next question that arises is regarding the viability of this route in more astronomically representative ice mixing ratios. To date, there are no convincing detections of H<sub>2</sub>S in interstellar ices, with upper limits estimated to be  $\leq 0.7\%$  with respect to water (Jiménez-Escobar & Muñoz Caro 2011). This would translate to ice abundance upper limits of roughly a few percent with respect to CO (e.g.,  $N(\text{H}_2\text{S})/N(\text{CO}) \lesssim 0.035$  if assuming  $N(\text{CO})/N(\text{H}_2\text{O}) \sim 0.21$  according to the median CO ice abundance value w.r.t H<sub>2</sub>O derived for low-mass young stellar objects (LYSOs) in Boogert et al. 2015). Accordingly, similar depositions with larger fractions of CO with respect to H<sub>2</sub>S are performed to assess how the dilution of the latter affects the yields of OCS. The deposition fluxes of H<sub>2</sub>S and atomic H are kept the same in all experiments, with only variations in the CO flux (see Table 1). Figure 3 compares the relative intensities of the OCS signals obtained from both the IR and QMS data for the different mixing ratios explored here (i.e., CO:H<sub>2</sub>S = 1:1, 5:1, 10:1, and 20:1). The areas of the OCS  $\nu_1$  vibrational modes for each mixing ratio after deposition are normalized to that of experiment 1, which yielded the largest absolute amount of products. Similarly, the areas of the  $m/z = 60$  desorption band at  $\sim 89$  K are also normalized to that of experiment 1.

Overall, the infrared and QMS data provide consistent OCS yields within their respective error bars, and signal that dilution of H<sub>2</sub>S in CO reduces, but does not impede OCS formation under our experimental conditions. Indeed, in the highest dilution case (5% H<sub>2</sub>S w.r.t. CO), OCS production diminishes by  $\sim 50\%$  (the mean value between the infrared and QMS results) in comparison to the non-diluted reference experiment (100% H<sub>2</sub>S w.r.t. CO). This decrease in OCS yield is likely governed by the reduced number of available H atoms in experiments with larger CO fractions, as opposed to a diminishing effectiveness of the OCS formation. As well established by previous works, the in-

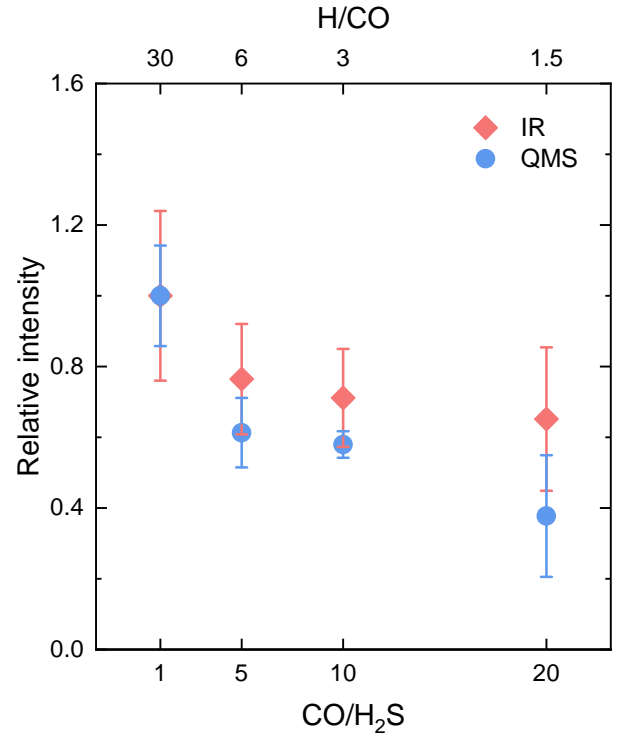


**Fig. 3.** Integrated intensities of the infrared and QMS features of OCS for different flux conditions: CO:H<sub>2</sub>S = 1:1, 5:1, 10:1, and 20:1. The infrared value is derived from the area of the  $\nu_1$  mode of OCS, while the QMS counterpart is calculated from the integrated desorption band for  $m/z = 60$  peaking at  $\sim 89$  K. The resulting yields are normalized to that of experiment 1 (CO:H<sub>2</sub>S = 1:1). The upper x-axis shows the corresponding ratios of H/CO, signaling the decrease in H-atom availability with increasing CO fractions.

teraction of CO with H atoms in the solid state initiates a chain of reactions leading to H<sub>2</sub>CO and CH<sub>3</sub>OH (Tielens & Hagen 1982; Charnley et al. 1992; Hiraoka et al. 1994; Watanabe & Kouchi 2002; Fuchs et al. 2009; Santos et al. 2022), which efficiently consumes the available atomic hydrogen in the system. Increasing the CO deposition flux while maintaining a fixed H-atom flux, therefore, results in less hydrogen being able to react with other species. This decrease in available H atoms will impact more significantly the formation of SH radicals (Reaction 5a) than the final abstraction step (Reaction 7), since the latter is predicted to proceed barrierlessly (Adriaens et al. 2010), whereas the former requires quantum tunneling through a barrier of  $\sim 1500$  K (Lamberts & Kästner 2017). The slowly decreasing trend in Figure 3 suggests that OCS can still be formed at 10 K in ice mixtures with CO:H<sub>2</sub>S higher than 20:1 and H:CO as low as 1.5:1. The formation of OCS from CO+SH could therefore have a non-negligible contribution to the observed OCS in interstellar ices, as discussed below.

## 4. Astrophysical implications

The reaction network probed in this work is shown in Figure 4. Aside from OCS, other closed-shell species also formed within this network are H<sub>2</sub>S<sub>2</sub> (Santos et al. 2023), H<sub>2</sub>CO and CH<sub>3</sub>OH (Tielens & Hagen 1982; Charnley et al. 1992; Hiraoka et al. 1994; Watanabe & Kouchi 2002; Fuchs et al. 2009; Santos et al. 2022). In our experiments, H<sub>2</sub>S is utilized as a source of SH radicals via a hydrogen abstraction (Reaction 5a) to avoid reactions with S atoms to interfere with the analysis. In the in-

terstellar medium, however, SH will not only be produced from  $\text{H}_2\text{S}$ , but also from the hydrogenation of sulfur atoms that adsorb onto dust grains (Reaction 3). Observations of singly- and doubly-deuterated  $\text{H}_2\text{S}$  in Class 0 sources suggest that the bulk of its formation takes place early in the evolution of a cloud, before the catastrophic CO freeze-out stage begins (Ceccarelli et al. 2014). Accordingly, SH radicals will be available in the ice as early as during the low-density pre-stellar core stage. As the cloud evolves and the density of the environment increases, most of the available S atoms will be converted into  $\text{H}_2\text{S}$ . Nonetheless, SH radicals can still be formed through Reaction 5a or through dissociation reactions induced by energetic processing. As a result, SH will remain a viable reactant throughout a large fraction of a cloud's lifetime.

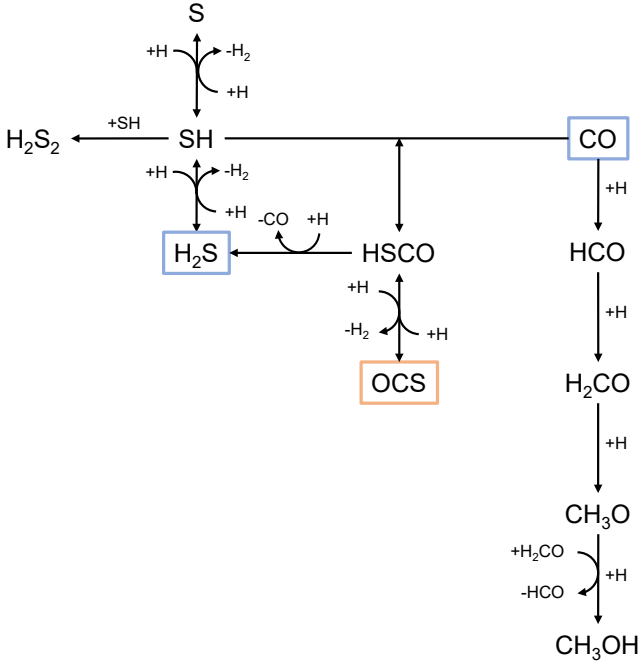


**Fig. 4.** Reaction scheme proposed in this work. Blue boxes denote the deposited molecules and the orange box highlights the studied product, OCS. Hydrogen abstraction reactions from  $\text{CH}_3\text{OH}$ ,  $\text{H}_2\text{CO}$ , and associated radicals are omitted for the sake of simplicity.

Observations of OCS towards massive young stellar objects (MYSOs) reveal that its  $4.9\ \mu\text{m}$  feature is best fitted by reference spectra of OCS in a  $\text{CH}_3\text{OH}$ -rich environment (Palumbo et al. 1997; Boogert et al. 2022). Their column density ratios ( $N(\text{OCS})/N(\text{CH}_3\text{OH})$ ) in both ice and gas have similarly narrow distributions and comparable median values (within a factor of 3, Santos et al. submitted), strengthening the hypothesis that both coexist in similar ice environments. Moreover, observed ice abundances of OCS and  $\text{CH}_3\text{OH}$  are correlated (Boogert et al. 2022), suggesting a strong chemical link between the two molecules. Since methanol is known to be formed via the hydrogenation of CO in the solid phase, such observations are in line with CO being a common precursor between the two. This would imply that the bulk of OCS ice likely originates deep into dense clouds, in a dense environment post catastrophic CO freeze-out. Conversely, a large portion of the free sulfur atoms will likely be readily converted into  $\text{H}_2\text{S}$  at such densities. The reaction route proposed here could partially circumvent this issue since SH radicals can be efficiently produced through a top-down mechanism (Reaction 5a). Moreover, estimated  $\text{H}_2\text{S}$  upper limits in ices are

larger than the detected OCS abundances (Palumbo et al. 1997; Jiménez-Escobar & Muñoz Caro 2011; Boogert et al. 2022), and thus this route remains viable in light of the observational evidence available so far. Overall, both  $\text{CO} + \text{S}$  and  $\text{CO} + \text{SH}$  routes are likely to be contributing to the observed OCS abundances in interstellar ices, the extent to which warrants dedicated chemical modeling to be constrained.

## 5. Conclusions

In this work, we conduct a systematic experimental investigation on the viability of forming OCS under dark cloud conditions from ice mixtures of CO,  $\text{H}_2\text{S}$ , and H atoms. Our main findings are summarized below:

- OCS can be efficiently formed at 10 K from solid-state reactions involving CO,  $\text{H}_2\text{S}$  and H. The proposed underlying mechanism is via  $\text{CO} + \text{SH} \rightarrow \text{HSCO}$  followed by  $\text{HSCO} + \text{H} \rightarrow \text{OCS} + \text{H}_2$ , analogously to  $\text{CO}_2$  ice.
- The OCS product yield decreases slowly with increasing initial  $\text{CO}/\text{H}_2\text{S}$  ratios and decreasing H-atom availability, resulting in  $\sim 50\%$  less OCS formation for a 20 times higher CO abundance relative to  $\text{H}_2\text{S}$  and fixed H-atom fluxes. This trend suggests that OCS can be efficiently formed via the proposed route in more representative interstellar ices where  $\text{H}_2\text{S}$  is likely highly diluted in CO.
- SH can be produced both through bottom-up ( $\text{S} + \text{H} \rightarrow \text{SH}$ ) and top-down ( $\text{H}_2\text{S} + \text{H} \rightarrow \text{SH} + \text{H}_2$ ) routes, thus making it a favorable reactant to form OCS during the high-density, post CO freeze-out stage of pre-stellar cores. This is in line with both ice and gas-phase observations of OCS in protostars.

These findings suggest that the  $\text{CO} + \text{SH}$  reaction is potentially responsible for a non-negligible share of the interstellar OCS ice and therefore could be a valuable new addition to gas-grain chemical models focused on sulfur species. In turn, such models could help to disentangle the contributions of the  $\text{CO} + \text{SH}$  and  $\text{CO} + \text{S}$  routes to forming OCS.

**Acknowledgements.** This work has been supported by the Danish National Research Foundation through the Center of Excellence “InterCat” (Grant agreement no.: DNRF150); the Netherlands Research School for Astronomy (NOVA); and the Dutch Astrochemistry Network II (DANII). KJC is grateful for support from NWO via a VENI fellowship (VI.Veni.212.296).

## References

- Adriaens, D., Goumans, T., Catlow, C., & Brown, W. 2010, *The Journal of Physical Chemistry C*, 114, 1892
- Altwegg, K., Combi, M., Fuselier, S. A., et al. 2022, *MNRAS*, 516, 3900
- Artur de la Villarmois, E., Guzmán, V. V., Yang, Y. L., Zhang, Y., & Sakai, N. 2023, *A&A*, 678, A124
- Biver, N., Bockelée-Morvan, D., Boissier, J., et al. 2021a, *A&A*, 648, A49
- Biver, N., Bockelée-Morvan, D., Lis, D. C., et al. 2021b, *A&A*, 651, A25
- Blake, G. A., Sutton, E. C., Masson, C. R., & Phillips, T. G. 1987, *ApJ*, 315, 621
- Blake, G. A., van Dishoeck, E. F., Jansen, D. J., Groesbeck, T. D., & Mundy, L. G. 1994, *ApJ*, 428, 680
- Bockelée-Morvan, D., Lis, D. C., Wink, J. E., et al. 2000, *A&A*, 353, 1101
- Boogert, A. C. A., Brewer, K., Brittain, A., & Emerson, K. S. 2022, *ApJ*, 941, 32
- Boogert, A. C. A., Gerakines, P. A., & Whittet, D. C. B. 2015, *ARA&A*, 53, 541
- Boogert, A. C. A., Schutte, W. A., Helmich, F. P., Tielens, A. G. G. M., & Wooden, D. H. 1997, *A&A*, 317, 929
- Booth, A. S., Temmink, M., van Dishoeck, E. F., et al. 2024, *AJ[arXiv:2402.04002]*
- Calmonte, U., Altwegg, K., Balsiger, H., et al. 2016, *MNRAS*, 462, S253
- Cartwright, R. J., Nordheim, T. A., Cruikshank, D. P., et al. 2020, *ApJ*, 902, L38
- Cazaux, S., Carrascosa, H., Muñoz Caro, G. M., et al. 2022, *A&A*, 657, A100



- Ceccarelli, C., Caselli, P., Bockelée-Morvan, D., et al. 2014, in *Protostars and Planets VI*, ed. H. Beuther, R. S. Klessen, C. P. Dullemond, & T. Henning, 859–882
- Cernicharo, J., Marcelino, N., Roueff, E., et al. 2012, *ApJ*, 759, L43
- Charnley, S. B., Tielens, A. G. G. M., & Millar, T. J. 1992, *ApJ*, 399, L71
- Chen, Y. J., Juang, K. J., Nuevo, M., et al. 2015, *ApJ*, 798, 80
- Codella, C., Bianchi, E., Podio, L., et al. 2021, *A&A*, 654, A52
- Drda, K., Knapp, G. R., & van Dishoeck, E. F. 1989, *ApJ*, 345, 815
- Drozdovskaya, M. N., van Dishoeck, E. F., Jørgensen, J. K., et al. 2018, *MNRAS*, 476, 4949
- Druard, C. & Wakelam, V. 2012, *MNRAS*, 426, 354
- Esplugues, G., Fuente, A., Navarro-Almáida, D., et al. 2022, *A&A*, 662, A52
- Esplugues, G. B., Viti, S., Goicoechea, J. R., & Cernicharo, J. 2014, *A&A*, 567, A95
- Fedoseev, G., Ioppolo, S., & Linnartz, H. 2015, *MNRAS*, 446, 449
- Ferrante, R. F., Moore, M. H., Spiliotis, M. M., & Hudson, R. L. 2008, *ApJ*, 684, 1210
- Fontani, F., Roueff, E., Colzi, L., & Caselli, P. 2023, *A&A*, 680, A58
- Fuchs, G. W., Cuppen, H. M., Ioppolo, S., et al. 2009, *A&A*, 505, 629
- Fuente, A., Cernicharo, J., Agúndez, M., et al. 2010, *A&A*, 524, A19
- Garozzo, M., Fulvio, D., Kanuchova, Z., Palumbo, M. E., & Strazzulla, G. 2010, *A&A*, 509, A67
- Garrod, R. T., Wakelam, V., & Herbst, E. 2007, *A&A*, 467, 1103
- Gibb, E., Nummelin, A., Irvine, W. M., Whittet, D. C. B., & Bergman, P. 2000, *ApJ*, 545, 309
- Goldsmith, P. F. & Li, D. 2005, *ApJ*, 622, 938
- Herpin, F., Marseille, M., Wakelam, V., Bontemps, S., & Lis, D. C. 2009, *A&A*, 504, 853
- Hibbitts, C. A., McCord, T. B., & Hansen, G. B. 2000, *J. Geophys. Res.*, 105, 22541
- Hiraoka, K., Ohashi, N., Kihara, Y., et al. 1994, *Chemical Physics Letters*, 229, 408
- Hudgins, D. M., Sandford, S. A., Allamandola, L. J., & Tielens, A. G. G. M. 1993, *ApJS*, 86, 713
- Ioppolo, S., Fedoseev, G., Lamberts, T., Romanzin, C., & Linnartz, H. 2013, *Rev. Sci. Instrum.*, 84, 073112
- Ioppolo, S., van Boheemen, Y., Cuppen, H. M., van Dishoeck, E. F., & Linnartz, H. 2011, *MNRAS*, 413, 2281
- Jessup, K. L., Spencer, J., & Yelle, R. 2007, *Icarus*, 192, 24
- Jiménez-Escobar, A. & Muñoz Caro, G. M. 2011, *Astronomy and Astrophysics*, 536, A91
- Jiménez-Escobar, A., Muñoz Caro, G. M., & Chen, Y. J. 2014, *MNRAS*, 443, 343
- Kolesníková, L., Tercero, B., Cernicharo, J., et al. 2014, *ApJ*, 784, L7
- Kushwahaa, T., Drozdovskaya, M. N., Tychoniec, Ł., & Tabone, B. 2023, *A&A*, 672, A122
- Laas, J. C. & Caselli, P. 2019, *A&A*, 624, A108
- Lacy, J. H., Knacke, R., Geballe, T. R., & Tokunaga, A. T. 1994, *ApJ*, 428, L69
- Lamberts, T. & Kästner, J. 2017, *The Journal of Physical Chemistry A*, 121, 9736, pMID: 29190103
- Le Gal, R., Öberg, K. I., Loomis, R. A., Pegues, J., & Bergner, J. B. 2019, *ApJ*, 876, 72
- Le Gal, R., Öberg, K. I., Teague, R., et al. 2021, *ApJS*, 257, 12
- Li, J., Wang, J., Zhu, Q., Zhang, J., & Li, D. 2015, *ApJ*, 802, 40
- Linke, R. A., Frerking, M. A., & Thaddeus, P. 1979, *ApJ*, 234, L139
- Loison, J.-C., Halvick, P., Bergeat, A., Hickson, K. M., & Wakelam, V. 2012, *MNRAS*, 421, 1476
- López-Gallifa, Á., Rivilla, V. M., Beltrán, M. T., et al. 2024, *MNRAS*, 529, 3244
- Majumdar, L., Gratier, P., Vidal, T., et al. 2016, *MNRAS*, 458, 1859
- McAnally, M., Bocková, J., Herath, A., et al. 2024, *Nature Communications*, 15, 4409
- McClure, M. K., Rocha, W. R. M., Pontoppidan, K. M., et al. 2023, *Nature Astronomy*, 7, 431
- Molpeceres, G., Enrique-Romero, J., & Aikawa, Y. 2023, *A&A*, 677, A39
- Molpeceres, G., García de la Concepción, J., & Jiménez-Serra, I. 2021, *ApJ*, 923, 159
- Moulet, A., Lellouch, E., Moreno, R., et al. 2013, *ApJ*, 776, 32
- Moulet, A., Lellouch, E., Moreno, R., Gurwell, M. A., & Moore, C. 2008, *A&A*, 482, 279
- Müller, H. S. P., Belloche, A., Xu, L.-H., et al. 2016, *A&A*, 587, A92
- Navarro-Almáida, D., Le Gal, R., Fuente, A., et al. 2020, *A&A*, 637, A39
- Nguyen, T., Oba, Y., Sameera, W. M. C., Kouchi, A., & Watanabe, N. 2021, *ApJ*, 922, 146
- Noble, J. A., Dulieu, F., Congiu, E., & Fraser, H. J. 2011, *ApJ*, 735, 121
- Oba, Y., Tomaru, T., Kouchi, A., & Watanabe, N. 2019, *ApJ*, 874, 124
- Oba, Y., Tomaru, T., Lamberts, T., Kouchi, A., & Watanabe, N. 2018, *Nature Astronomy*, 2, 228
- Oba, Y., Watanabe, N., Kouchi, A., Hama, T., & Pirronello, V. 2010, *ApJ*, 712, L174
- Öberg, K. I., Boogert, A. C. A., Pontoppidan, K. M., et al. 2008, *ApJ*, 678, 1032
- Oya, Y., Sakai, N., López-Sepulcre, A., et al. 2016, *ApJ*, 824, 88
- Palumbo, M. E., Geballe, T. R., & Tielens, A. G. G. M. 1997, *ApJ*, 479, 839
- Palumbo, M. E., Tielens, A. G. G. M., & Tokunaga, A. T. 1995, *ApJ*, 449, 674
- Phuong, N. T., Chapillon, E., Majumdar, L., et al. 2018, *A&A*, 616, L5
- Qasim, D., Lamberts, T., He, J., et al. 2019, *A&A*, 626, A118
- Qasim, D., Witlox, M. J. A., Fedoseev, G., et al. 2020, *Rev. Sci. Instrum.*, 91, 054501
- Rivière-Marichalar, P., Fuente, A., Le Gal, R., et al. 2021, *A&A*, 652, A46
- Rocha, W. R. M., van Dishoeck, E. F., Ressler, M. E., et al. 2024, *A&A*, 683, A124
- Rodríguez-Almeida, L. F., Jiménez-Serra, I., Rivilla, V. M., et al. 2021, *ApJ*, 912, L11
- Santos, J. C., Chuang, K.-J., Lamberts, T., et al. 2022, *ApJ*, 931, L33
- Santos, J. C., Linnartz, H., & Chuang, K. J. 2023, *A&A*, 678, A112
- Santos, J. C., van Gelder, M. L., Nazari, P., Ahmadi, A., & van Dishoeck, E. F. submitted, *A&A*
- Semenov, D., Favre, C., Fedele, D., et al. 2018, *A&A*, 617, A28
- Shingledecker, C. N., Lamberts, T., Laas, J. C., et al. 2020, *ApJ*, 888, 52
- Smith, A. M., Stecher, T. P., & Casswell, L. 1980, *ApJ*, 242, 402
- Spezzano, S., Sipilä, O., Caselli, P., et al. 2022, *A&A*, 661, A111
- Tielens, A. G. G. M. & Hagen, W. 1982, *A&A*, 114, 245
- Tschersich, K. G. 2000, *J. Appl. Phys.*, 87, 2565
- van der Tak, F. F. S., Boonman, A. M. S., Braakman, R., & van Dishoeck, E. F. 2003, *A&A*, 412, 133
- Vidal, T. H. G., Loison, J.-C., Jaziri, A. Y., et al. 2017, *MNRAS*, 469, 435
- Wang, J., Marks, J. H., Tuli, L. B., et al. 2022, *The Journal of Physical Chemistry A*, 126, 9699
- Watanabe, N. & Kouchi, A. 2002, *ApJ*, 571, L173
- Yarnall, Y. Y. & Hudson, R. L. 2022, *ApJ*, 931, L4
- Zapata, L. A., Palau, A., Galván-Madrid, R., et al. 2015, *MNRAS*, 447, 1826